Geophysical Research Letters

RESEARCH LETTER
10.1029/2025GL120445

Adsorption Preceding Wetting Front Controls Seismic Velocity

Rui Wu[1,2], Hongpu Kang[1,2], Fuqiang Gao[1,2], Xiangyuan Peng[1,2], Shuangyong Dong[1,2], Chenxi Zhao[1,2], Bing Qiuyi Li[3], Kerry Leith[4], Qinghua Lei[5], Gennady Y. Gor[6], Paul A. Selvadurai[7], and Xiaoping Jia[8]

[1]CCTEG Coal Mining Research Institute, Beijing, China, [2]State Key Laboratory of Intelligent Coal Mining and Strata Control, Beijing, China, [3]Department of Civil and Environmental Engineering, Western University, London, ON, Canada, [4]Earth Sciences New Zealand, Lower Hutt, New Zealand, [5]Department of Earth Sciences, Uppsala University, Uppsala, Sweden, [6]Otto H. York Department of Chemical and Materials Engineering, New Jersey Institute of Technology, NEWARK, NJ, USA, [7]Swiss Seismological Service, Department of Earth and Planetary Sciences, ETH Zürich, Zürich, Switzerland, [8]Institut Langevin, ESPCI Paris, Université PSL, CNRS, Paris, France

Abstract Rock elasticity varies with both humidity and water saturation, yet their combined effects remain poorly understood, although in nature vapor adsorption and liquid infiltration occur simultaneously. Here, we present experimental data of P-wave velocity and volume expansion in a free-standing sandstone subject to progressive wetting. Elastic softening, evidenced by P-wave velocity reduction, precedes the wetting front, followed by stiffening as liquid infiltration reverses this trend. To reconcile these softening/stiffening behaviors, vapor migration ahead of the wetting front is captured by numerical simulation of moisture transport constrained by experimental data. Initial softening is explained by a micromechanical model governed by surface energy reduction at grain contacts and validated by independent vapor adsorption tests. Subsequent stiffening is attributed to water infiltration, consistent with patchy saturation theory. We propose softening and stiffening are transitional processes governed by the advancing wetting front, with implications for seismic imaging of progressive wetting processes in crustal rocks.

Plain Language Summary Rocks near Earth's surface contain both liquid water and water vapor in their pores. When water enters during wetting, the rock responds in two distinct stages: vapor first adsorbs onto grain surfaces ahead of infiltrating water, softening the rock at all scales. Then, air is replaced by water in the pores, causing the rock to stiffen. We study this process in the laboratory by tracking P-wave velocity and sample deformation during progressive wetting. This is supported by vapor adsorption tests, micromechanical models and numerical simulations. Results show sequential softening and stiffening as the wetting front advances, explaining why seismic signals often appear muted despite strong hydrological forcing. Given that seismic velocities are the most common way to image the subsurface, these findings recontextualize seismic velocity changes responding to hydro-mechanical forcing, with implications for subsurface problems such as groundwater management, geothermal, nuclear waste disposal, and energy storage.

Key Points:

- Laboratory measurements track vapor adsorption zone preceding wetting front, where elastic softening occurs
- Micromechanical model relates adsorption-induced elastic softening to volume expansion of rocks
- Moisture dynamics drives a continuous transition from adsorption-induced softening to saturation-induced stiffening

Supporting Information:

Supporting Information may be found in the online version of this article.

Correspondence to:

F. Gao,
fuqgao@gmail.com

Citation:

Wu, R., Kang, H., Gao, F., Peng, X., Dong, S., Zhao, C., et al. (2026). Adsorption preceding wetting front controls seismic velocity. *Geophysical Research Letters*, *53*, e2025GL120445. https://doi.org/10.1029/2025GL120445

Received 4 NOV 2025
Accepted 6 APR 2026

Author Contributions:

Conceptualization: Rui Wu, Hongpu Kang, Fuqiang Gao
Funding acquisition: Hongpu Kang, Fuqiang Gao
Investigation: Rui Wu, Xiangyuan Peng, Shuangyong Dong, Chenxi Zhao, Gennady Y. Gor
Methodology: Xiangyuan Peng, Shuangyong Dong, Chenxi Zhao
Project administration: Hongpu Kang, Fuqiang Gao
Supervision: Hongpu Kang, Fuqiang Gao, Bing Qiuyi Li, Kerry Leith, Qinghua Lei, Paul A. Selvadurai, Xiaoping Jia
Writing – original draft: Rui Wu, Bing Qiuyi Li, Kerry Leith

1. Introduction

Crustal rocks at or near Earth's surface are typically unsaturated, with water present as both liquid and vapor. The moisture content of crustal rocks is regulated by boundary conditions derived from their climatic, geomorphological, and geothermal settings. Spontaneous imbibition, or progressive wetting, is a two-phase flow process in which capillary forces drive liquid water to displace air (Zahasky & Benson, 2019). Changes in moisture content have been shown to affect the elastic properties of near-surface bedrock (Eppes et al., 2020), with implications for water management, natural hazards, and engineering activity. Examples include seismic velocity changes linked to groundwater dynamics (Mao et al., 2022), geothermal steam accumulation (Sánchez-Pastor et al., 2023), underground energy storage (Zoback & Smit, 2023), and nuclear waste disposal (Rutqvist & Tsang, 2012). These wetting-associated elastic changes have previously been imaged through tomography using near-surface seismic waves that are inherently sensitive to pore fluids (liquid and vapor) (Kramer et al., 2023; Solazzi et al., 2021; Whiteley et al., 2019).

However, the wetting process is complex, as water vapor can migrate faster than liquid infiltration via adsorption and subsequent capillary condensation at pore walls and grain contacts (Zahasky & Benson, 2019). As a result,

Writing – review & editing: Rui Wu, Hongpu Kang, Fuqiang Gao, Bing Qiuyi Li, Kerry Leith, Qinghua Lei, Gennady Y. Gor, Paul A. Selvadurai, Xiaoping Jia

vapor tends to advance ahead of the wetting front, creating zones of contrasting saturation that produce different elastic responses. This creates two distinct regimes. On the one hand, liquid infiltration produces elastic stiffening at high water saturation (e.g., tens of %), as pore filling increases the effective elastic moduli (Mavko et al., 1998). On the other hand, vapor adsorption, occurring at very low water saturation (e.g., a few percent), leads to elastic softening. Adsorbed films can reduce mineral surface energy (Bangham's law) (Bangham & Fakhoury, 1928; Gor et al., 2017; Parks, 1984), bonding strength, and consequently their stiffness at grain contacts (Johnson et al., 1971). The collective weakening of these contacts decreases effective elastic moduli at the macroscopic scale, with reported wave velocity reductions of 5%–30% (Murphy et al., 1984; Pimienta et al., 2014; Yurikov et al., 2018). Thus, liquid infiltration and vapor adsorption generally exert competing effects on rock elasticity (stiffening vs. softening), which is nominally proportional to the square of wave velocity. This contrast is poorly resolved in field-scale measurements, where ray paths often pass through and therefore average across both competing regimes, obscuring clear velocity changes (Mao et al., 2022; Sánchez-Pastor et al., 2023). Such averaging introduces errors in inverted hydrogeological profiles, leading to apparent homogeneity despite strong subsurface heterogeneities.

In recent decades, extensive laboratory studies have investigated elastic changes during progressive wetting, primarily through wave velocity measurements (David, Barnes, et al., 2017; David et al., 2015; David, Sarout, et al., 2017; Geremia et al., 2021; Lopes et al., 2014; Pimienta et al., 2019; Wulff & Mjaaland, 2002). While rooted in rock physics, these efforts align with broader work in material physics on capillary and adsorption effects (Sanchez et al., 2024). However, key gaps remain that limit our ability to isolate adsorption-induced softening from progressive wetting. Only a few studies have directly delineated the wetting front using X-ray imaging (David et al., 2015; Sanchez et al., 2024) or surface deformation mapping (Wu, Selvadurai, Li, Leith, et al., 2023; Wu, Selvadurai, Li, Sun, et al., 2023); most others lack this resolution. While elastic softening has been attributed to vapor adsorption, previous studies have not quantified or mapped the adsorption zone ahead of the wetting front, nor evaluated its contribution to the overall elastic response (David, Sarout, et al., 2017; Lopes et al., 2014). Both progressive wetting and vapor adsorption lead to changes in wave velocity and volumetric strain (Wu, Selvadurai, Li, Leith, et al., 2023; Wu, Selvadurai, Li, Sun, et al., 2023), but the relationship between them has not yet been investigated explicitly, leaving the role of vapor adsorption unresolved. Moreover, adsorption and wetting are often investigated separately, even though they represent a continuous spectrum in which one gradually transitions into the other (Zahasky & Benson, 2019). Overall, the limited availability of targeted data and integrated modeling approaches has constrained efforts to disentangle adsorption-induced softening from progressive wetting effects.

Here, we monitor spontaneous imbibition in sandstone through simultaneous measurements of P-wave velocity and bulk volume change via optical surface deformation, supported by independent material characterization tests that isolate vapor effects from liquid infiltration. Experimental data on adsorption-induced elastic softening/stiffening and bulk volume expansion are reconciled within an analytical micromechanical model at the grain-contact scale, along with finite element simulations of moisture transport. We show that adsorption-induced softening precedes and gradually transitions to water saturation-driven stiffening as the wetting front advances. The integration of laboratory experiments, analytical modeling, and numerical simulations explains how subtle vapor adsorption preceding liquid infiltration at the pore scale cascades into macroscopic changes in seismic velocity.

2. Materials and Methods

2.1. Material Characterization

Tests are performed on white sandstone, which has been well characterized (Wu et al., 2025). Thin section reveals an arkosic composition consisting of approximately 70% quartz, 25% feldspar, and 5% rock fragments. The sandstone is fine-grained with an average grain size of 240 μm. Grain and bulk densities are measured at 2.50 g/cm^3 and 2.26 g/cm^3, respectively. Porosity is determined to be 9.13 ± 0.07% through combined mercury intrusion and nuclear magnetic resonance techniques, and 9.05 ± 0.008% through vacuum saturation. The pore size distribution is bimodal: a macropore population centered around 2.5 μm and a nanopore population below 100 nm (Thommes et al., 2015). Based on surface area analysis, approximately 85% of the nanopores fall within the 4–20 nm range. Matrix permeability for water flow is approximately 2.9×10^{-16} m^2. P-wave velocity under oven-dried and water-saturated conditions is measured to be 3160 ± 10 m/s and 3762 ± 14 m/s, respectively.

10.1029/2025GL120445

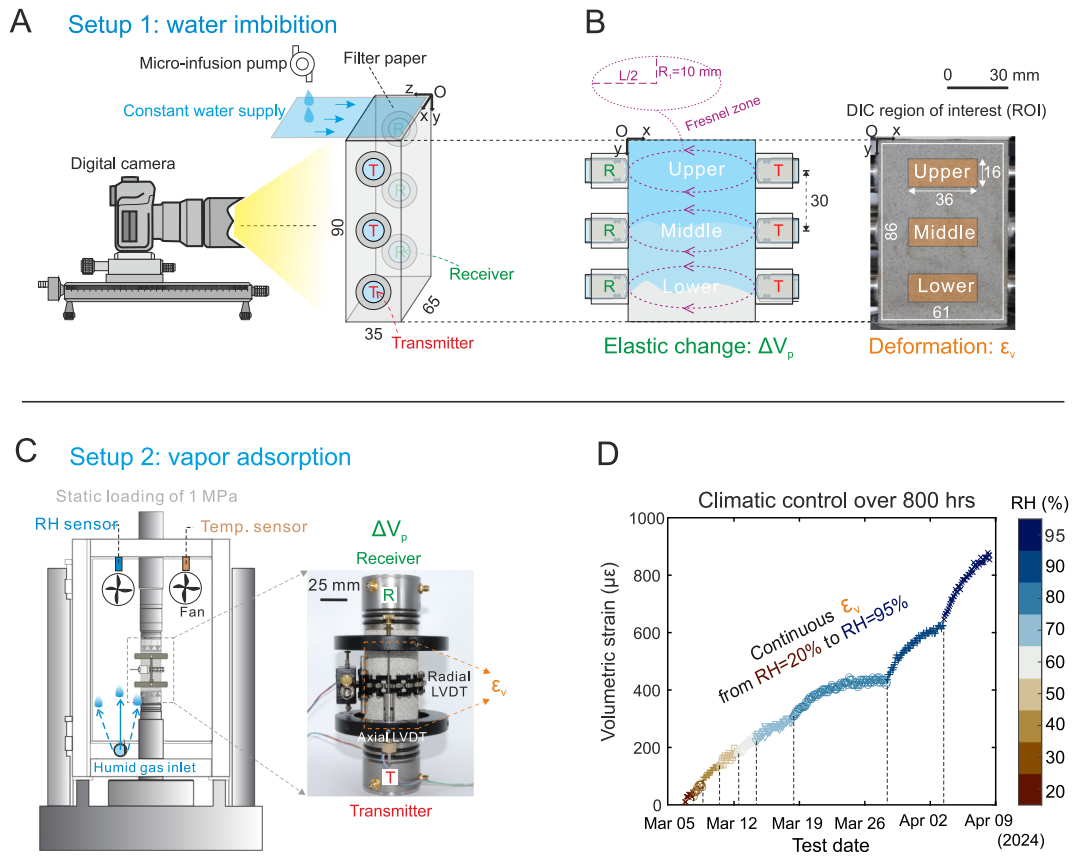

Figure 1. Overview of experimental setups and conditions for measuring moisture-induced elastic changes and deformation. (a) Setup 1: Schematic of the water imbibition experiment, where a free-standing sandstone prism is progressively wetted from the top over 80 hr. (b) Monitoring configuration for ultrasonic and digital image correlation measurements. Three transmitter–receiver (T–R) pairs are mounted along the sides of the specimen to track changes in P-wave velocity (Δv_p). A digital camera captures the front face for volumetric strain (ε_v) mapping, with a defined region of interest subdivided into Upper, Middle, and Lower zones corresponding to P-wave Fresnel zones determined by T-R pairs. (c) Setup 2: Schematic of the vapor adsorption experiment, where a cylindrical specimen is subjected to uniaxial compression (1 MPa) inside a climatic chamber. Relative humidity (RH) and temperature are precisely controlled. Ultrasonic measurements are conducted axially for changes in P-wave velocity (Δv_p), and global volumetric strain (ε_v) is measured using axial and radial LVDTs. (d) Volumetric strain in response to the climatic protocol of 9 staged relative humidities (20, 30, 40, 50, 60, 70, 80, 90, and 95%) at constant temperature (25°C) over 800 hr. The volumetric strain shows continuous expansion, with color indicating RH level.

2.2. Experimental Setup for Spontaneous Water Imbibition

We conduct water imbibition tests on an intact prismatic sandstone specimen (Figure 1a, dimension: 65 × 35 × 90 mm) held in a free-standing configuration. The specimen is first oven-dried at 80°C, and then acclimated to laboratory ambient conditions (see environmental record in Figure S3a of Supporting Information S1) for 16 hr. Water is then introduced to the top surface using a layer of filter paper, which is continuously supplied with distilled water by a micro-infusion pump over an 80-hr period, while the bottom surface is in contact with a metal base.

As shown in Figure 1b, we employ time-lapse ultrasound and digital image correlation techniques to simultaneously investigate changes in elastic properties and sample deformation during progressive wetting. Three pairs of ultrasonic transmitters (T) and receivers (R), referred to as the Upper, Middle, and Lower pairs, are mounted on opposite sides of the specimen with a vertical spacing of 30 mm, spanning the specimen from top to bottom. Each transmitter emits a pulse every minute using a 500 V excitation voltage (Selvadurai et al., 2022; Wu et al., 2021). Here, we focus on P-wave analysis, as reliable S-wave arrivals cannot be resolved due to masking by earlier P-wave energy. Concurrently, images of the frontal surface of the specimen are captured every 5 min with a digital

camera, a rate chosen to limit data volume while remaining sufficient to resolve the smoothly evolving deformation at this timescale.

The obtained images are processed to track the vertical progression of the wetting front and to measure the sample deformation in the form of in-plane horizontal strain ε_{xx} and vertical strain ε_{yy}. We assume a vertically advancing wetting front that promotes comparable lateral expansional strains in both horizontal directions. Accordingly, the out-of-plane strain along the specimen thickness is approximated by ε_{xx}, yielding the volumetric strain $\varepsilon_v = 2\varepsilon_{xx} + \varepsilon_{yy}$. Deviations from an ideal flat wetting front (e.g., uneven advancement) may introduce uncertainty into volumetric strain estimates, but are not expected to influence overall deformation trends.

We aim to link P-wave velocity changes Δv_p with local volumetric strain ε_v. As illustrated in Figure 1b, the spatial sensitivity of each T-R pair is defined by a confocal prolate ellipsoidal region, known as the P-wave first Fresnel zone (P-FFZ), within which the direct wave response is most sensitive to elastic changes (David, Sarout, et al., 2017; Spetzler & Snieder, 2004). We define the minor axis length R_1 of the P-FFZ as $R_1 = \frac{1}{2}\sqrt{\lambda L + \frac{\lambda^2}{4}}$, where λ is the wavelength and L is the T-R distance (65 mm). We determine an upper frequency for spectral analysis as 500 kHz so that R_1 is estimated to be no wider than 8 mm. To evaluate ε_v from the image data, we define rectangular regions (36 × 16 mm) centered on each P-FFZ and compute the spatial average within these zones. A vertical spacing of 30 mm between T-R pairs is maintained to prevent overlap between adjacent P-FFZs. To clarify the acoustic and optical techniques and the definition of the wetting front, we provide additional analysis and tests (Texts S1–S3 and Figures S1–S3 in Supporting Information S1).

2.3. Experimental Setup for Water Vapor Adsorption

To quantify the effect of vapor adsorption on rock elasticity at the specimen scale, we expose a cylindrical sandstone sample of diameter 50 mm and length 100 mm to controlled relative humidity (RH). P-wave velocity along the axial direction and the sample deformation on the lateral surface are monitored as RH is varied. As shown in Figure 1c, the specimen is placed under uniaxial compression inside a climatic chamber capable of controlling RH with an accuracy of ±0.8%. P-wave velocity is measured using an ultrasonic T-R pair positioned at the specimen ends, while axial and radial LVDTs record volumetric strain. These LVDTs are independently calibrated for the testing range of RH. A constant axial load of 1 MPa is applied to ensure consistent ultrasonic transmission across the specimen–transducer interfaces, as lower loads produced insufficient signal-to-noise ratios under elevated humidity. This stress level is negligible relative to the material strength and does not induce measurable creep, as the observed deformation is dominated by immediate adsorption-induced expansion rather than time-dependent mechanical shortening.

Figure 1d illustrates that the RH is increased incrementally across nine stages from 20% (orange) to 95% (blue) over a total period of 800 hr. Throughout the test, the temperature is held constant at 25 ± 0.1°C. The duration of each RH step is determined based on the stabilization of volumetric strain, which is considered positive due to the dominant expansion response. Each RH stage is maintained for at least 48 hr following equilibrium before advancing to the next level. Detailed LVDT calibration, creep assessment, and verification of ultrasonic velocity stability at each RH step are provided in the (Texts S4–S6 and Figures S3–S6 in Supporting Information S1).

3. Results

3.1. Spontaneous Water Imbibition

We investigate the physical response of a white sandstone during spontaneous water imbibition using setup 1. Changes in P-wave velocity (Δv_p) are shown in Figure 2a across three P-wave first Fresnel zones (P-FFZs), referred to as Upper, Middle, and Lower, from top to bottom of the specimen. Time zero marks when water is introduced to the top surface. In all three regions, Δv_p initially decreases, then increases after reaching a minimum, and eventually stabilizes. While the magnitude and timing of Δv_p differ across regions, the overall trend is consistent. The voltage waveforms recorded across three P-FFZs are provided in Figure S1 of Supporting Information S1.

To examine how elastic changes relate to deformation, we present vertical strain (ε_{yy}) and volumetric strain (ε_v) on the front face of the specimen in Figures 2b and 2c. These maps are shown at key moments: the time of

10.1029/2025GL120445

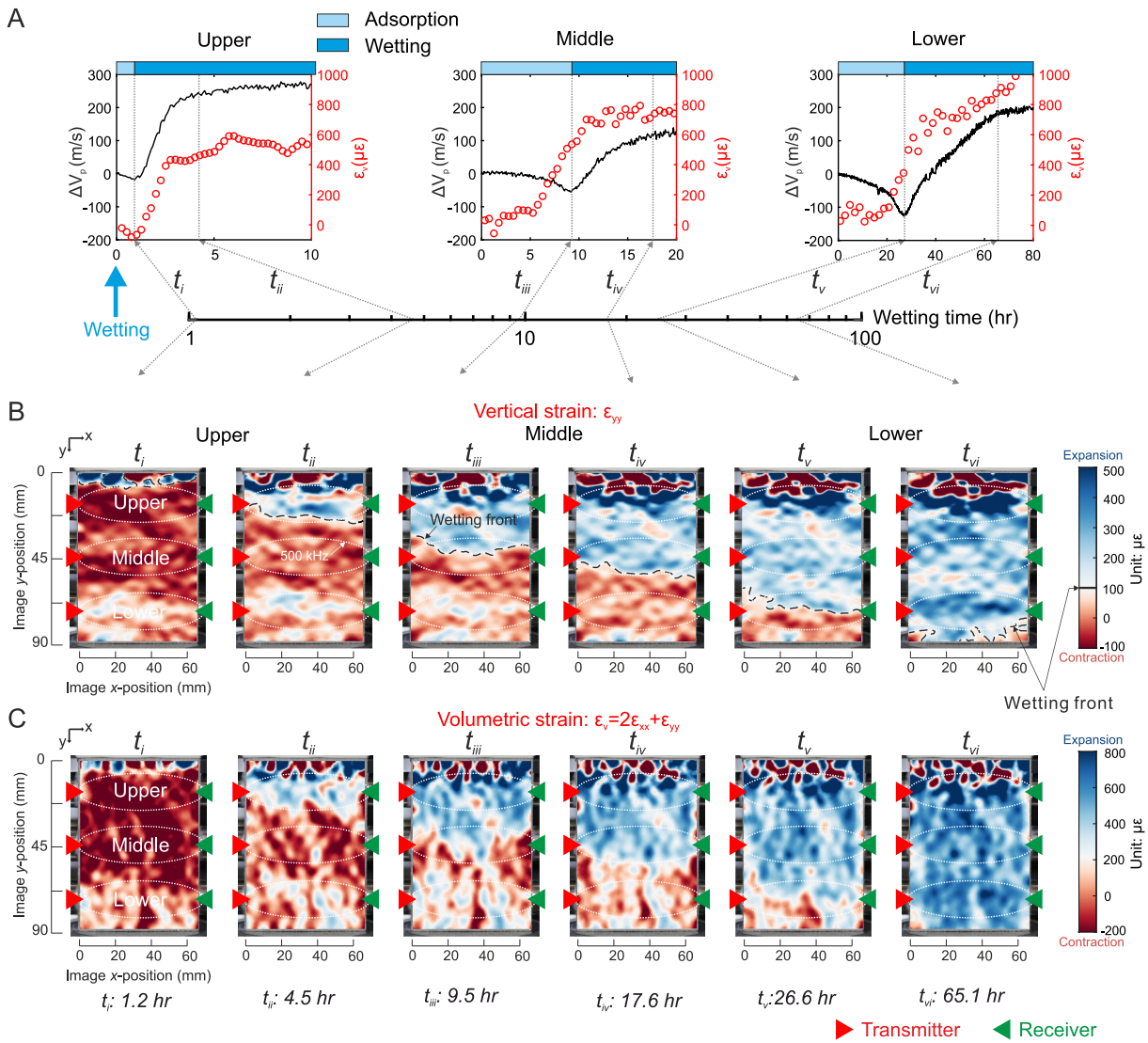

Figure 2. Spontaneous water imbibition test (setup 1). (a) Temporal evolution of P-wave velocity changes (black line) for the Upper, Middle, and Lower regions of the specimen. Red circles show volumetric strain (ε_v) calculated within each region. (b) Vertical strain (ε_{yy}) and (c) volumetric strain ($\varepsilon_v = 2\varepsilon_{xx} + \varepsilon_{yy}$) maps on the front face of the specimen at selected times. Red and blue indicate contraction and expansion, respectively. Transmitter and receiver locations are marked by red and green arrows.

maximum velocity reduction (t_i, t_{iii}, t_v) and the time that the wetting front passes the lower boundary of each zone (t_{ii}, t_{iv}, t_{vi}). Blue and red indicate expansion and contraction, respectively. The movement of the wetting front is visualized using the 100 $\mu\varepsilon$ vertical strain threshold, described in Text S3 and further justified in the later section. P-FFZs are represented as ellipses with a minor axis of approximately 8 mm at 500 kHz. The average volumetric strain (ε_v) in each P-FFZ is computed and shown as red circles in Figure 2a.

Following water introduction, the acousto-mechanical response shows a consistent transition from softening (Δv_p as low as −124 m/s) to stiffening (Δv_p up to +299 m/s) as the wetting front sequentially advances across the specimen. Note that the measured velocity variations (several percent) far exceed the estimated uncertainty (around 0.26%) from moisture-induced expansion (Text S7 in Supporting Information S1). Meanwhile, the specimen exhibits net volumetric expansion throughout the experiment. A summary of the acoustic and mechanical responses throughout the imbibition process is given in Table S2 of Supporting Information S1.

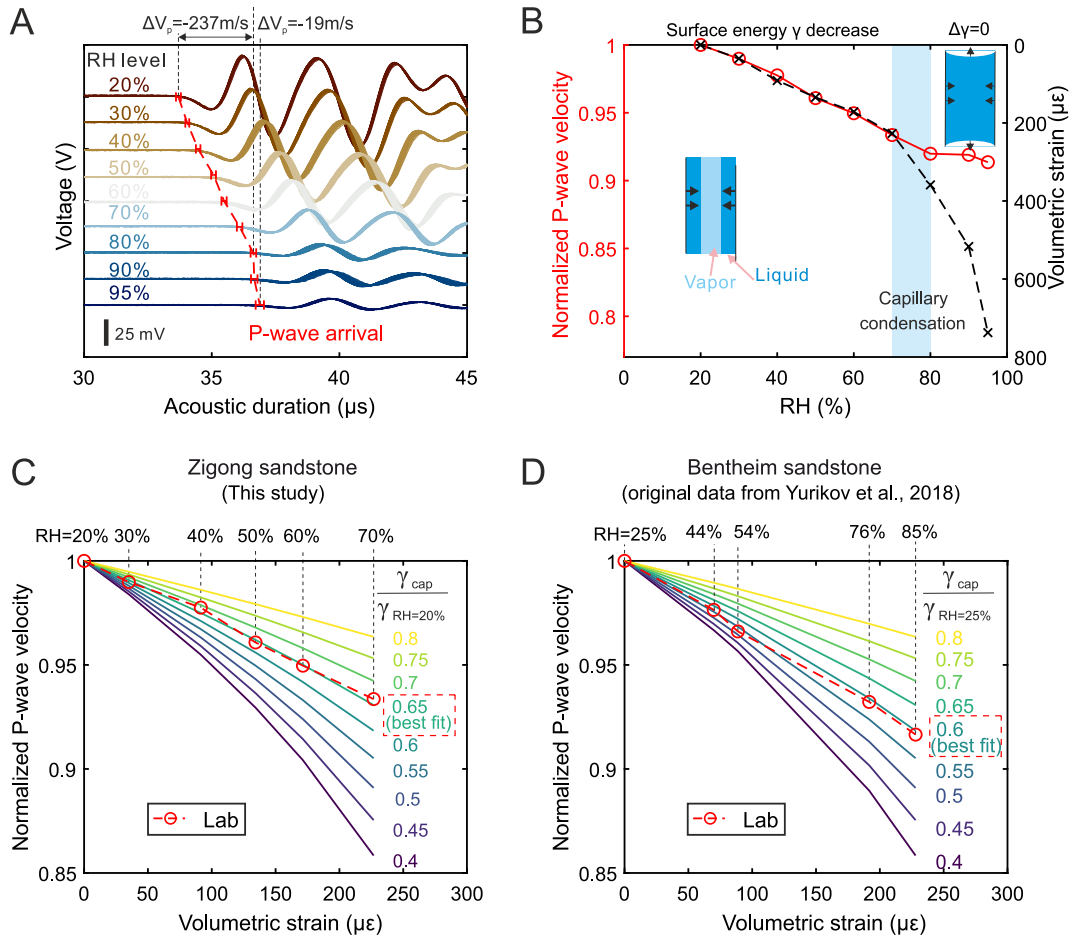

Figure 3. Water vapor adsorption test (setup 2) under staged RH levels. (a) Stacked ultrasonic waveforms near the P-wave arrival, recorded at RH levels from 20% to 95%. Red markers indicate picked arrival times. Color tones (orange to blue) correspond to increasing RH. (b) Normalized P-wave velocity (red circles) and corresponding volumetric strain (black crosses) as functions of RH. Insets illustrate the transition from vapor adsorption to capillary condensation. (c), (d) Comparison between experimental data (red circles) and model predictions of normalized P-wave velocity as a function of volumetric strain, based on (3). Results are shown for Zigong sandstone (C, this study) and Bentheim sandstone (D, reanalyzed from (Yurikov et al., 2018)).

3.2. Water Vapor Adsorption

To isolate vapor adsorption effects on rock elasticity independently from liquid infiltration, we conduct tests using setup 2, in which the sandstone specimen is equilibrated at staged relative humidity (RH) levels from 20% to 95%. Figure 3 shows the corresponding acoustic and mechanical responses. Figure 3a illustrates the direct waveforms near the P-wave arrival (with red cross), where orange and blue tones indicate low and high RH levels, respectively. As RH increases, P-wave arrivals shift progressively later, indicating slower wave velocities along the specimen axis. Overall, P-wave velocity (v_p) decreases by approximately 237 m/s (or 8%) from RH = 20%–80%, followed by a smaller reduction of 19 m/s (0.6%) from 80% to 95%. The observed velocity changes (up to several percent) are well above the uncertainty (around 0.15%) from moisture-induced expansion (Text S7 in Supporting Information S1).

To relate wave velocity changes to mechanical deformation, we compare the normalized v_p with the corresponding volumetric strain ε_v as a function of RH (Figure 3b). Both metrics exhibit nearly linear trends up to RH = 70%, where v_p decreases by 7% but ε_v increases only by 227 $\mu\varepsilon$ (around 0.023%). This behavior is consistent with the trends reported for clay-free sandstones, where v_p reductions of 9%–14% and ε_v on the order of several hundred microstrain have been observed as RH approaches 80% (Clark et al., 1980; Pimienta et al., 2014;

Yurikov et al., 2018). These observations indicate that the wave velocity reduction is significantly greater than the volume expansion caused by vapor adsorption.

Given the observed acoustic and mechanical responses (Figure 3b), we interpret RH ranging between 70% and 80% as the onset of capillary condensation beyond which vapor condenses into liquid form within nanopores, leading to significant volumetric expansion (Gor et al., 2017; Wu et al., 2025). At RH below this threshold, elastic softening is primarily attributed to reduced surface energy (Gregg & Sing, 1982).

4. Discussion

4.1. Coupling Between Adsorption-Induced Deformation and Elastic Softening

Both the water imbibition test and vapor adsorption test indicate correlated elastic softening and volumetric expansion with increasing moisture content. Specifically, this is observed ahead of the wetting front in the imbibition test, and at RH below capillary condensation in the adsorption test. This similarity, consistent with previous studies (David, Sarout, et al., 2017; Israelachvili, 2011), suggests that vapor migration near grain surfaces precedes liquid infiltration and induces elastic changes through adsorption. To quantify this effect, we derive an analytical relationship between P-wave velocity (v_p) and volumetric strain (ε_v), validate it using vapor adsorption measurements, and then apply it to interpret the imbibition data.

We model the sandstone as a granular assembly of cemented monodisperse spherical grains with identical radius and elastic properties (Canel et al., 2024; Digby, 1981; Walton, 1987). At the grain scale, both normal and tangential contact stiffness (k) is described using Johnson–Kendall–Roberts (JKR) theory, which applies to elastic adhesive contacts. Within this framework, k is controlled by the external load and adhesive interactions through surface energy (γ). Under negligible external load and in the absence of initial bonding, JKR theory predicts $k \propto \gamma$ (Johnson et al., 1971). When upscaling to the macroscopic behaviors, we assume that no new grain contacts form during deformation, grain centers deform consistently within a uniform strain field, the packing is dense, and the grain spatial distribution is statistically homogeneous and random. Under these conditions, the effective compressional or shear modulus M scales linearly with contact stiffness, $M \propto k$ (Walton, 1987). Because M is proportional to the square of wave velocity (Mavko et al., 1998) and here P-wave velocity v_p is measured, we obtain $v_p^6 \propto \gamma$, leading to

$$\frac{\gamma_1}{\gamma_0} = \left(\frac{v_{p,1}}{v_{p,0}}\right)^6, \tag{1}$$

where subscripts 0 and 1 denote the initial and final humidity states prior to capillary condensation. During vapor adsorption, simultaneous volumetric expansion represents an averaged macroscopic response of a porous solid containing nanoscale adsorption sites. This behavior is described by Bangham's law (Bangham & Fakhoury, 1928), for review see also (Gor et al., 2017), which relates volumetric strain to reductions in surface energy, such that $\varepsilon_v|_0^1 \propto \Delta\gamma|_0^1$. Although JKR theory and Bangham's law were developed for different length scales (i.e., granular contact vs. nanopore below 100 nm), they are considered to be compatible here because the sandstone is granular in nature while also containing nanopores where vapor adsorption occurs. Together, these mechanisms allow adsorption-induced expansion to be quantitatively linked to elastic softening. Assuming the surface energy is not changing beyond the capillary condensation:

$$\frac{\varepsilon_v}{\varepsilon_v^{cap}} = \frac{\gamma_0 - \gamma_1}{\gamma_0 - \gamma_{cap}}, \tag{2}$$

where ε_v^{cap} and γ_{cap} represent the volumetric strain and surface energy at the capillary condensation point. Combining Equations 1 and 2, we obtain an analytical expression that links normalized v_p to adsorption-induced deformation:

$$\frac{v_{p,\,1}}{v_{p,\,0}} = \left[1 - \left(1 - \frac{\gamma_{cap}}{\gamma_0}\right)\frac{\varepsilon_v}{\varepsilon_v^{cap}}\right]^{1/6}. \tag{3}$$

To verify this relationship, we compare predicted and measured normalized P-wave velocities based on volumetric strain data from both Zigong sandstone (this study) and Bentheim sandstone (Yurikov et al., 2018), a medium-grained, quartz-rich rock. We use $\varepsilon_v^{cap} = 227\ \mu\varepsilon$ for Zigong sandstone, corresponding to volumetric expansion from RH = 20%–70% (Figure 3b), and $\varepsilon_v^{cap} = 228\ \mu\varepsilon$ for Bentheim sandstone, from RH = 25%–85% (Yurikov et al., 2018), both representing volumetric expansion up to the capillary condensation point. Figures 3c and 3d present the predicted $v_p/v_{p,0}$ (solid lines) for γ_{cap}/γ_0 ranging from 0.4 to 0.8. Best agreement with the experimental data is found at $\gamma_{cap}/\gamma_0 \approx 0.65$ for Zigong sandstone and 0.60 for Bentheim sandstone (see residuals in Figure S8 of Supporting Information S1). A complete overview of P-wave velocity and volumetric strain across all tested RH levels for both sandstones is provided in Figure S9 of Supporting Information S1.

The fitted parameter γ_{cap}/γ_0 is consistent with the expected range for quartz-dominated materials. Reported surface energy ratios between vapor-saturated and dry hydroxylated quartz surfaces range from approximately 0.66 to 0.85, depending on surface treatment and experimental conditions (Parks, 1984). The slightly lower value observed for Bentheim sandstone may reflect its higher RH at capillary condensation (85%) compared to Zigong sandstone (70%), resulting in a more modest surface energy reduction. This close agreement between model predictions and experimental data supports the proposed framework, indicating that it effectively captures the coupling between adsorption-induced deformation and elastic softening, mediated by grain-scale surface energy reduction.

4.2. Unifying Adsorption and Wetting

We test the hypothesis that vapor adsorption occurs ahead of the wetting front and drives elastic softening before liquid infiltration-induced stiffening. Specifically, adsorption and wetting are treated here as a continuous spectrum of moisture dynamics rather than as separate regimes. We develop a 3D finite element simulation of the evolution of water saturation (S_w) and RH level during spontaneous imbibition. Liquid transport follows Darcy's law, expressed for unsaturated flow, driven by capillary and gravitational forces (Alava et al., 2004; Washburn, 1921). Vapor transport kinetics is represented indirectly by one-way coupling, where RH is inferred from S_w using the equilibrium thermodynamic relationship measured in a water vapor adsorption isotherm test. The simulation configuration represents the experimental imbibition setup. The top surface is maintained at $S_w = 1$ to represent a constant water source, the lateral surfaces exchange mass with ambient air at 40% RH, and the bottom surface is treated as no-flux by contact with a metal base. The simulation framework is described in detail (see Text S8, Figures S10 and S11 of Supporting Information S1) and is validated against independent experimental benchmarks (Text S9, Figures S12–S14 in Supporting Information S1).

Figure 4a shows the simulated S_w and RH at six time instants corresponding to those in Figure 2. Black dashed contours represent S_w, while red solid contours indicate RH. Notably, the RH transition zone of 80 ± 5% aligns closely with the vertical strain-based wetting front defined by the 100 $\mu\varepsilon$ contour (green dashed line; see also Figure 2b).

From the vapor adsorption measurements (Figure 3b), an RH increase from 40% (ambient) to 80 ± 5% generates an additional volumetric expansion of 267 ± 70 $\mu\varepsilon$. Assuming isotropic deformation in this homogeneous sandstone under low axial stress (1 MPa), the volumetric expansion is approximated as three times the single strain component. This component, measured at 89 $\mu\varepsilon$, is consistent with the 100 $\mu\varepsilon$ threshold used to track the wetting front. Note that this first-order assumption links adsorption-induced expansion to imbibition-induced deformation while neglecting minor stress-induced anisotropy. These findings support the use of RH = 80 ± 5% as a simulated wetting front in terms of the amount of vapor adsorbed onto the pore walls.

With the wetting dynamics quantified, we focus on the acoustic and mechanical responses in the Lower region (orange crosses in Figure 4b), which shows the strongest elastic softening (with a velocity reduction of −124 m/s), about seven times greater than in the Upper (−18 m/s) and twice that in the Middle region (−55 m/s). This pronounced response likely results from a more diffuse vapor front in the lower region, making it the most suitable zone for isolating the effects of vapor adsorption.

Softening persists until time t_v, when the wetting front, identified from either the model (RH = 80 ± 5%) or strain measurements, has passed through Lower zone. During this interval, simulated RH remains at or below 80 ± 5%, and no stiffening is observed. We therefore assume the response is solely attributed to vapor adsorption at grain contacts caused by a reduction in surface energy. Applying the developed velocity–strain relationship from

10.1029/2025GL120445

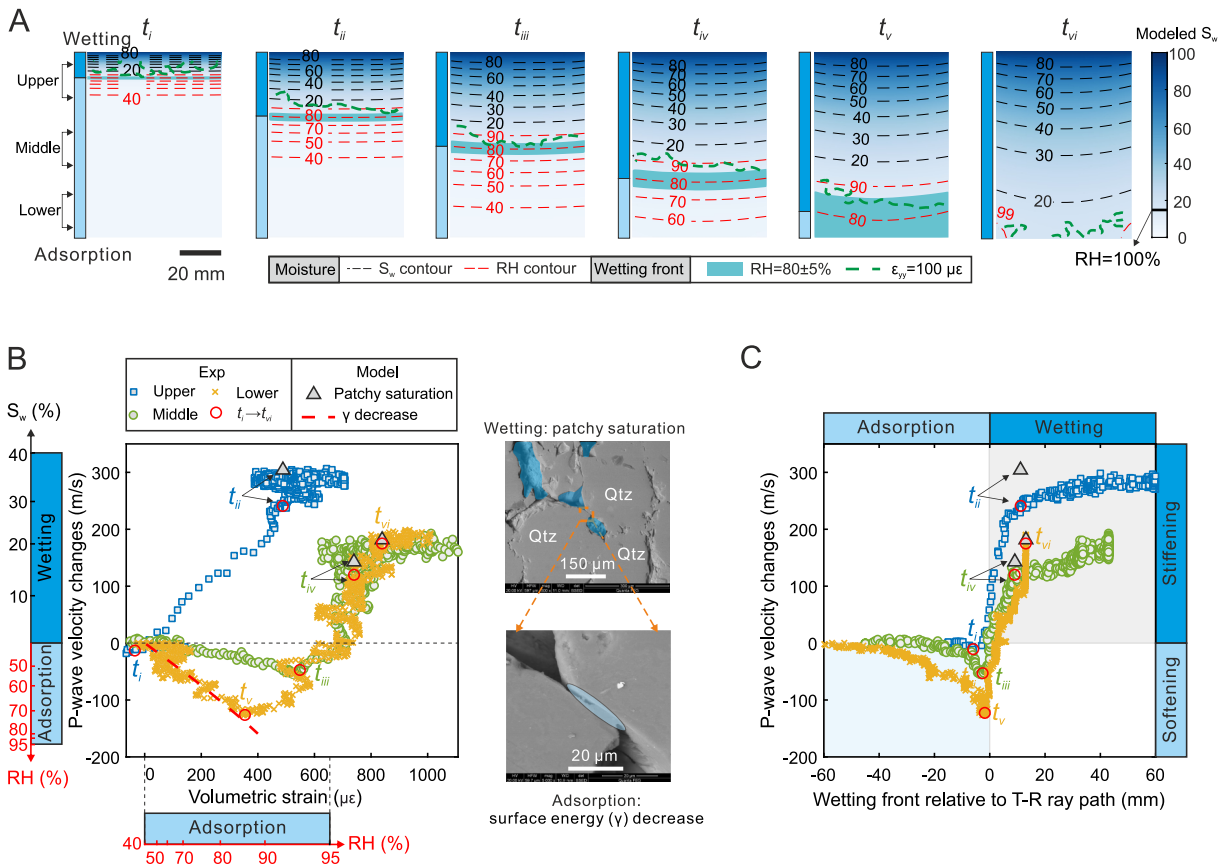

Figure 4. Spatiotemporal evolution of moisture content and elastic response as the wetting front progresses through the Upper, Middle, and Lower regions of the specimen. (a) Simulated contours of water saturation (S_w) and relative humidity (RH) at six representative times (t_i to t_{vi}), plotted along the specimen height. The shaded band indicates the simulated wetting front, defined by RH = 80 ± 5%, is shown together with the strain-based wetting front inferred from the ϵ_{yy} = 100 με contour (green dashed line). (b) Measured P-wave velocity changes plotted against volumetric strain in each zone. Red circles denote transition points from velocity decrease to increase. Corresponding RH levels (40%–95%) are added, derived from the velocity–strain data set in Figure 3B. SEM images illustrate distinct mechanisms driving the observed elastic changes: stiffening from patchy saturation (top) and softening from surface energy reduction (bottom). (c) P-wave velocity changes as a function of the strain-based wetting front position relative to the transmitter–receiver ray path. A consistent trend from softening to stiffening is observed as the front approaches and moves through each zone.

(Equation 3) to the measured volumetric expansion (up to 316 ± 36 με) predicts a reduction in velocity that closely matches the observed magnitude and trend (red dashed line). To better constrain the role of vapor adsorption, RH levels (40%–95%) are added to the axis of Figure 4b using the velocity–strain data set from Figure 3b. From this scaling, the Lower region is estimated to have experienced an RH increase from ambient (40%) to slightly above 80% before time t_v.

4.3. Elastic Property Evolution Across the Wetting Front

In the previous section, we attributed the elastic softening in Figure 4b to vapor adsorption ahead of liquid water. Equally important, however, is the subsequent stiffening, where v_p begins to rise in all zones after times t_{ii}, t_{iv}, and t_{vi}. This transition occurs as the wetting front, identified by simulated RH above 80 ± 5% or measured vertical strains exceeding 100 με, advances through each zone.

In the Lower zone, a clear reversal from softening to stiffening is observed at time t_v, after which v_p increases by 314 m/s relative to its minimum value, as simulated S_w rises from 10.5% to 20% (Figure S12 in Supporting Information S1). Similar increases occur in the Upper zone between times t_i and t_{ii} (+262 m/s) and in the Middle zone between times t_{iii} and t_{iv} (+160 m/s). Notably, v_p at the Middle zone shows the most pronounced spatial transition between softening in Lower zone and stiffening in Upper zones. These observed stiffening responses are possibly due to the effect of the replacement of air and vapor by liquid water on passing elastic waves.

To examine this effect, we conducted independent hydrostatic compression tests on dry and fully saturated sandstones to isolate the effect of liquid pore water on wave velocity. The measured P and S-wave velocities closely match Gassmann's predictions (Gassmann, 1951) over a confining pressure range of 1–55 MPa, with a maximum mismatch of 50 m/s. This agreement indicates that wave-induced fluid pressure is effectively equilibrated during ultrasonic wave propagation, consistent with a quasi-static elastic response enabled by sufficient pore connectivity under saturated conditions.

Accordingly, we predict velocity changes under partial saturation using simulated water saturation (S_w) values according to patchy saturation theory (Gurevich et al., 2024; Mavko et al., 1998). This theory assumes that the rock consists of spatial patches with different local saturation. Within each patch, fluid pressure is equilibrated and elastic moduli follow Gassmann's predictions for the local effective fluid, while pressure equilibration between patches does not occur over the wave period. The shear modulus is therefore assumed constant and identical to the dry value, and velocity changes arise from saturation-dependent variations in the bulk modulus. This framework predicts a monotonic increase in P-wave velocity with increasing S_w, which we compare directly with measured stiffening during imbibition. Details of the hydrostatic compression tests, along with predictions from Gassmann's and patchy saturation theories, are provided in the (Texts S10 and S11, Figures S15 and S16 of Supporting Information S1).

Because no direct strain–stiffening relation exists in porous rocks, we compare velocity changes with the position of the wetting front relative to the T–R ray path (Figure 4c). Across all zones, velocities first decline when the front remains distant, reflecting adsorption-induced softening, and then rise once the front intersects the ray path, reflecting wetting-induced stiffening. When the wetting front leaves the P-FFZs, simulated saturation supports this interpretation: S_w is approximately 38% in the Upper, 19.4% in the Middle, and 21.5% in the Lower zone. When these values are used in patchy saturation theory, the predicted velocity increases agree well with the measurements (gray triangles in Figures 4b and 4c).

4.4. Implications for Seismic Velocity Variations During Progressive Wetting

In this study, the advancing wetting front produces a 4.2% decrease in seismic velocity due to adsorption-induced softening, followed by a 10% increase associated with saturation-induced stiffening within the same unsaturated region, resulting in a net velocity increase of less than 6%. This sequence is consistent with prior laboratory studies of progressive wetting, which report precursory elastic softening caused by vapor diffusion ahead of the liquid front, with velocity reductions up to 20%, followed by stiffening of similar magnitude once the wetting front traverses the seismic sensing volume (David, Sarout, et al., 2017; Geremia et al., 2021; Lopes et al., 2014; Pimienta et al., 2019). Our results extend these observations by explicitly resolving how softening and stiffening coexist and evolve within the same unsaturated region as wetting progresses, rather than appearing as separate stages.

Although this study focuses on a quartz-rich, clay-free sandstone to ensure reproducibility and minimize chemical effects, the underlying mechanisms are expected to apply broadly to unsaturated porous rocks where vapor and liquid coexist. Adsorption-induced softening and wetting-induced stiffening arise from micromechanical processes at grain contacts and pore surfaces, and therefore represent generic elastic responses to moisture redistribution. The magnitude of these effects, however, depends on transport properties, mineralogy, and microstructure, which together govern the relative roles of vapor diffusion and liquid infiltration.

Permeability and vapor diffusivity are important in controlling the prominence of adsorption-related precursors. In the present sandstone (permeability 2.9×10^{-16} m^2), vapor diffusion ahead of the wetting front produces pronounced elastic softening prior to infiltration-induced stiffening. In contrast, low-permeability crystalline rocks such as Herrnholz granite $\left(7.4 \times 10^{-19}\ \mathrm{m}^2\right)$ exhibit negligible adsorption-induced softening before stiffening occurs (Wu, Selvadurai, Li, Leith, et al., 2023). Mineralogy, surface chemistry, and microstructure further modulate this behavior. For instance, clay-bearing sandstones, with higher surface area and hydrophilicity, show amplified adsorption effects and larger velocity reductions with increasing humidity (Tiennot & Fortin, 2020), whereas carbonate rocks, characterized by well-cemented microstructures and fully bonded grain contacts, display only minor humidity-related velocity changes (Clark et al., 1980; Pimienta et al., 2014).

By documenting the coexistence of elastic softening and stiffening during progressive wetting, this study clarifies the origin of seismic velocity variations in vadose zones, such as those associated with oscillations of the capillary

fringe (Mao et al., 2022), which often appear small despite strong hydrological forcing. Our findings also help reinterpret seismic velocity variations in geothermal reservoirs where steam caps evolve from vapor–liquid redistribution (Sánchez-Pastor et al., 2023). Beyond these settings, the results are relevant to underground energy storage, where injected hydrogen, CO_2 or compressed air coexist with residual water, influencing the acoustic and mechanical response of the reservoir and providing a means to infer gas occupancy or detect leakage through seismic monitoring (Zoback & Smit, 2023).

5. Conclusions

To conclude, we have presented experimental results, together with micromechanical contact models and numerical simulation of moisture transport, demonstrating that progressive wetting reconciles elastic changes between wave velocity and mechanical deformation through two distinct but related mechanisms. Ahead of the wetting front, elastic softening is evidenced by P-wave velocity reduction and volumetric expansion when vapor adsorbs onto grain surfaces and contacts along the triple gas–solid–liquid interface. This reduces grain-grain adhesion (bonding) and contact stiffness, producing measurable softening accompanied by volumetric expansion. As pores become progressively filled with capillary-driven liquid water, this trend reverses and stiffening dominates, consistent with simulated wetting dynamics and patchy saturation theory. These findings reveal how subtle pore-scale processes cascade into measurable, macroscopic elastic changes when vapor migration precedes the wetting front. Our work highlights the critical role of progressive wetting in controlling the seismic response of crustal rocks, with important implications for various near-surface and subsurface problems.

Conflict of Interest

The authors declare no conflicts of interest relevant to this study.

Availability Statement

Data in this study is available on Zenodo and can be downloaded from Wu (2025).

Acknowledgments

R.W., F.G., and X.P. are financially supported by the National Natural Science Foundation of China (Grant 52325403), CCTEG Coal Mining Research Institute (Grants KCYJY-2024-SYS-01, KCYJY-2026-QN-05). K.L. is financially supported by the Ministry of Business, Innovation and Employment (MBIE) under the 2022 Endeavour Fund Research Programmes (Grant UOCX2207). B.Q.L. is supported by NSERC Discovery Grant RGPIN-2022-03917. Q.L. is grateful for the financial support from State Key Laboratory of Intelligent Coal Mining and Strata Control (Grant SKLIS202418). We acknowledge valuable discussions on (a) wetting dynamics modeling with Professor Boris Gurevich, and (b) implications for groundwater fluctuation monitoring with Professor Shujuan Mao, Professor Yixiao Sheng, and Dr. Jinwu Li.

References

Alava, M., Dubé, M., & Rost, M. (2004). Imbibition in disordered media. *Advances in Physics*, *53*(2), 83–175. https://doi.org/10.1080/00018730410001687363

Bangham, D., & Fakhoury, N. (1928). The expansion of charcoal accompanying sorption of gases and vapours. *Nature*, *122*(3079), 681–682. https://doi.org/10.1038/122681b0

Canel, V., Jia, X., Campillo, M., & Ionescu, I. (2024). Acoustic monitoring of compaction in cohesive granular materials. *Physical Review E - Statistical Physics, Plasmas, Fluids, and Related Interdisciplinary Topics*, *109*(2), 24902. https://doi.org/10.1103/PhysRevE.109.024902

Clark, V. A., Tittmann, B. R., & Spencer, T. W. (1980). Effect of volatiles on attenuation (Q -1) and velocity in sedimentary rocks. *Journal of Geophysical Research*, *85*(B10), 5190–5198. https://doi.org/10.1029/JB085iB10p05190

David, C., Barnes, C., Desrues, M., Pimienta, L., Sarout, J., & Dautriat, J. (2017). Ultrasonic monitoring of spontaneous imbibition experiments: Acoustic signature of fluid migration. *Journal of Geophysical Research: Solid Earth*, *122*(7), 4931–4947. https://doi.org/10.1002/2016JB013804

David, C., Bertauld, D., Dautriat, J., Sarout, J., Menéndez, B., & Nabawy, B. (2015). Detection of moving capillary front in porous rocks using X-ray and ultrasonic methods. *Frontiers in Physics*, *3*, 53. https://doi.org/10.3389/fphy.2015.00053

David, C., Sarout, J., Dautriat, J., Pimienta, L., Michée, M., Desrues, M., & Barnes, C. (2017). Ultrasonic monitoring of spontaneous imbibition experiments: Precursory moisture diffusion effects ahead of water front. *Journal of Geophysical Research: Solid Earth*, *122*(7), 4948–4962. https://doi.org/10.1002/2017JB014193

Digby, P. J. (1981). The effective elastic moduli of porous granular rocks. *Journal of Applied Mechanics*, *48*(4), 803–808. https://doi.org/10.1115/1.3157738

Eppes, M. C., Magi, B., Scheff, J., Warren, K., Ching, S., & Feng, T. (2020). Warmer, wetter climates accelerate mechanical weathering in field data, independent of stress-loading. *Geophysical Research Letters*, *47*(24), 2020GL089062. https://doi.org/10.1029/2020GL089062

Gassmann, F. (1951). Elastic waves through a packing of spheres. *Geophysics*, *16*(4), 673–685. https://doi.org/10.1190/1.1437718

Geremia, D., David, C., Ismail, R., & El Haitami, A. (2021). An integrated study of water weakening and fluid rock interaction processes in porous rocks: Linking mechanical behavior to surface properties. *Applied Sciences*, *11*(23), 11437. https://doi.org/10.3390/app112311437

Gor, G. Y., Huber, P., & Bernstein, N. (2017). Adsorption-induced deformation of nanoporous materials—A review. *Applied Physics Reviews*, *4*(1), 11303. https://doi.org/10.1063/1.4975001

Gregg, S. J., & Sing, K. S. W. (1982). *Adsorption surface area and porosity*. Academic Press.

Gurevich, B., Nzikou, M. M., & Gor, G. Y. (2024). Modeling patchy saturation of fluids in nanoporous media probed by ultrasound and optics. *Physical Review E - Statistical Physics, Plasmas, Fluids, and Related Interdisciplinary Topics*, *109*(6), 64801. https://doi.org/10.1103/PhysRevE.109.064801

Israelachvili, J. N. (2011). *Intermolecular and surface forces*. Academic Press.

Johnson, K. L., Kendall, K., Roberts, A. D., & Tabor, D. (1971). Surface energy and the contact of elastic solids. *Proceedings of the Royal Society of London. A. Mathematical and Physical Sciences*, *324*(1558), 301–313. https://doi.org/10.1098/rspa.1971.0141

Kramer, R., Lu, Y., & Bokelmann, G. (2023). Interaction of air pressure and groundwater as main cause of sub-daily relative seismic velocity changes. *Geophysical Research Letters*, *50*(7), e2022GL101298. https://doi.org/10.1029/2022GL101298

Lopes, S., Lebedev, M., Müller, T. M., Clennell, M. B., & Gurevich, B. (2014). Forced imbibition into a limestone: Measuring P-wave velocity and water saturation dependence on injection rate. *Geophysical Prospecting*, *62*(5), 1126–1142. https://doi.org/10.1111/1365-2478.12111

Mao, S., Lecointre, A., van der Hilst, R. D., & Campillo, M. (2022). Space-time monitoring of groundwater fluctuations with passive seismic interferometry. *Nature Communications*, *13*(1), 4643. https://doi.org/10.1038/s41467-022-32194-3

Mavko, G., Mukerji, T., & Dvorkin, J. (1998). *The rock physics handbook*. Cambridge University Press. https://doi.org/10.1017/9781108333016

Murphy, W. F. I., Winkler, K. W., & Kleinberg, R. L. (1984). Frame modulus reduction in sedimentary rocks: The effect of adsorption on grain contacts. *Geophysical Research Letters*, *11*(9), 805–808. https://doi.org/10.1029/GL011i009p00805

Parks, G. A. (1984). Surface and interfacial free energies of quartz. *Journal of Geophysical Research*, *89*(B6), 3997–4008. https://doi.org/10.1029/JB089iB06p03997

Pimienta, L., David, C., Sarout, J., Perrot, X., Dautriat, J., & Barnes, C. (2019). Evolution in seismic properties during low and intermediate water saturation: Competing mechanisms during water imbibition? *Geophysical Research Letters*, *46*(9), 4581–4590. https://doi.org/10.1029/2019GL082419

Pimienta, L., Fortin, J., & Guéguen, Y. (2014). Investigation of elastic weakening in limestone and sandstone samples from moisture adsorption. *Geophysical Journal International*, *199*(1), 335–347. https://doi.org/10.1093/gji/ggu257

Rutqvist, J., & Tsang, C.-F. (2012). Multiphysics processes in partially saturated fractured rock: Experiments and models from Yucca Mountain. *Reviews of Geophysics*, *50*(3). https://doi.org/10.1029/2012RG000391

Sanchez, J., Dammann, L., Gallardo, L., Li, Z., Fröba, M., Meißner, R. H., et al. (2024). Deformation dynamics of nanopores upon water imbibition. *Proceedings of the National Academy of Sciences*, *121*(38), e2318386121. https://doi.org/10.1073/pnas.2318386121

Sánchez-Pastor, P., Wu, S.-M., Hokstad, K., Kristjánsson, B., Drouin, V., Ducrocq, C., et al. (2023). Steam caps in geothermal reservoirs can be monitored using seismic noise interferometry. *Communications Earth & Environment*, *4*(1), 453. https://doi.org/10.1038/s43247-023-01122-8

Selvadurai, P. A., Wu, R., Bianchi, P., Niu, Z., Michail, S., Madonna, C., & Wiemer, S. (2022). A methodology for reconstructing source properties of a conical piezoelectric actuator using array-based methods. *Journal of Nondestructive Evaluation*, *41*(1), 23. https://doi.org/10.1007/s10921-022-00853-6

Solazzi, S. G., Bodet, L., Holliger, K., & Jougnot, D. (2021). Surface-wave dispersion in partially saturated soils: The role of capillary forces. *Journal of Geophysical Research: Solid Earth*, *126*(12), e2021JB022074. https://doi.org/10.1029/2021JB022074

Spetzler, J., & Snieder, R. (2004). The fresnel volume and transmitted waves. *Geophysics*, *69*(3), 653–663. https://doi.org/10.1190/1.1759451

Thommes, M., Kaneko, K., Neimark, A. V., Olivier, J. P., Rodriguez-Reinoso, F., Rouquerol, J., & Sing, K. S. W. (2015). Physisorption of gases, with special reference to the evaluation of surface area and pore size distribution (IUPAC technical report). *Pure and Applied Chemistry*, *87*(9–10), 1051–1069. https://doi.org/10.1515/pac-2014-1117

Tiennot, M., & Fortin, J. (2020). Moisture-induced elastic weakening and wave propagation in a clay-bearing sandstone. *Géotechnique Letters*, *10*(3), 424–428. https://doi.org/10.1680/jgele.19.00052

Walton, K. (1987). The effective elastic moduli of a random packing of spheres. *Journal of the Mechanics and Physics of Solids*, *35*(2), 213–226. https://doi.org/10.1016/0022-5096(87)90036-6

Washburn, E. W. (1921). The dynamics of capillary flow. *Phys. Rev.*, *17*(3), 273–283. https://doi.org/10.1103/PhysRev.17.273

Whiteley, J. S., Chambers, J. E., Uhlemann, S., Wilkinson, P. B., & Kendall, J. M. (2019). Geophysical monitoring of moisture-induced landslides: A review. *Reviews of Geophysics*, *57*(1), 106–145. https://doi.org/10.1029/2018RG000603

Wu, R. (2025). Data for the study adsorption preceding wetting front controls seismic velocity. *Zenodo*, *10*. https://doi.org/10.5281/zenodo.17367109

Wu, R., Kang, H., Gao, F., Li, B. Q., Leith, K., Lei, Q., et al. (2025). Interplay of loading and adsorption controls elastic deformation of clastic and crystalline rocks. *Geophysical Research Letters*, *52*(18), e2025GL117126. https://doi.org/10.1029/2025GL117126

Wu, R., Selvadurai, P. A., Chen, C., & Moradian, O. (2021). Revisiting piezoelectric sensor calibration methods using elastodynamic body waves. *Journal of Nondestructive Evaluation*, *40*(3), 68. https://doi.org/10.1007/s10921-021-00799-1

Wu, R., Selvadurai, P. A., Li, Y., Leith, K., Lei, Q., & Loew, S. (2023). Laboratory acousto-mechanical study into moisture-induced reduction of fracture stiffness in granite. *Geophysical Research Letters*, *50*(23), e2023GL105725. https://doi.org/10.1029/2023GL105725

Wu, R., Selvadurai, P. A., Li, Y., Sun, Y., Leith, K., & Loew, S. (2023). Laboratory acousto-mechanical study into moisture-induced changes of elastic properties in intact granite. *International Journal of Rock Mechanics and Mining Sciences*, *170*, 105511. https://doi.org/10.1016/j.ijrmms.2023.105511

Wulff, A., & Mjaaland, S. (2002). Seismic monitoring of fluid fronts: An experimental study. *Geophysics*, *67*(1), 221–229. https://doi.org/10.1190/1.1451622

Yurikov, A., Lebedev, M., Gor, G. Y., & Gurevich, B. (2018). Sorption-induced deformation and elastic weakening of Bentheim sandstone. *Journal of Geophysical Research: Solid Earth*, *123*(10), 8589–8601. https://doi.org/10.1029/2018JB016003

Zahasky, C., & Benson, S. M. (2019). Spatial and temporal quantification of spontaneous imbibition. *Geophysical Research Letters*, *46*(21), 11972–11982. https://doi.org/10.1029/2019GL084532

Zoback, M., & Smit, D. (2023). Meeting the challenges of large-scale carbon storage and hydrogen production. *Proceedings of the National Academy of Sciences*, *120*(11), e2202397120. https://doi.org/10.1073/pnas.2202397120

References From the Supporting Information

Blaber, J., Adair, B., & Antoniou, A. (2015). Ncorr: Open-source 2D digital image correlation Matlab software. *Experimental Mechanics*, *55*(6), 1105–1122. https://doi.org/10.1007/s11340-015-0009-1

Gurevich, B., Makarynska, D., de Paula, O. B., & Pervukhina, M. (2010). A simple model for squirt-flow dispersion and attenuation in fluid-saturated granular rocks. *Geophysics*, *75*(6), N109–N120. https://doi.org/10.1190/1.3509782

Taylor, J. (1997). *Introduction to error analysis, the study of uncertainties in physical measurements*. University Science Books.